

Importance of bond exchange in MnC structural stability and half-metallic ferromagnetism: a comprehensive benchmark density functional study

Abdesalem Houari^{1,*} and Peter E. Blöchl²

¹*Theoretical Physics Laboratory, Department of Physics, University of Bejaia, Bejaia, Algeria*

²*Clausthal University of Technology, Institute for Theoretical Physics,
Leibnizstr.10, D-38678 Clausthal-Zellerfeld, Germany*

(Dated: November 25, 2025)

Recently, the first successful synthesis of bulk manganese monocarbide (MnC) has been reported. The compound crystallizes in the zincblende (B3) structure and has been proposed as a potential superhard material. In this work, we present a comprehensive first-principles study of the structural, electronic, and magnetic properties of MnC using several exchange–correlation approximations. We demonstrate that the SCAN meta-GGA and the PBE0r hybrid functional outperform GGA–PBESol, HSE06, and the mean-field DFT+ U + V schemes in correctly predicting the experimentally observed zincblende structure as the ground state. Our analysis reveals that the bond-exchange interaction plays a decisive role in stabilizing this phase. At theoretical equilibrium, hybrid functionals (PBE0r and HSE06) predict a metallic ground state, whereas semilocal functionals (PBESol and SCAN) and DFT+ U + V yield two distinct types of half-metallic ferromagnetism with opposite volume dependence, opening a debate on the origin and nature of this behavior. If confirmed experimentally, such a property would make MnC an attractive candidate for spintronic applications.

PACS numbers: 71.10.-w, 71.15.Mb, 71.15.Nc

Keywords: Transition-metal carbides, half-metallic ferromagnetism, DFT calculations, spintronics

I. INTRODUCTION

The stoichiometric binary mono-compounds arising from late $3d$ transition metal (Mn, Fe, Co, Ni and Cu) and light elements (C, N and O) show a variety of interesting physical properties. Among them, the monoxides (e.g. MnO, FeO, NiO), are well known since a long time and their properties are well established experimentally and theoretically^{1–4}. These systems, which crystallize in the rocksalt structure, have served for decades as benchmark materials for the study of strong correlations^{5,6}.

In contrast, the corresponding mononitrides remained more challenging experimentally until the end of the past century^{7–10}. For instance, the experimentally observed antiferromagnetic MnN, in a distorted rocksalt structure, is currently well established^{11,12}. On the other side, the crystal structure FeN and CoN was the subject of some debates^{13,14}, but it has been confirmed later that both adopt a zincblende one¹⁵. Finally, NiN and CuN remain experimentally unknown, and some *ab-initio* predictions of their ground state structure continue to disagree^{16–18}.

The situation is more complicated for monocarbides (MnC, FeC etc.) which are hardly known. Their difficult synthesis is mainly attributed to the progressive filling of the antibonding states along the late $3d$ series, which weakens the metal–carbon bonding and makes the stoichiometric phases highly unstable^{19–21}. Nevertheless, some *ab initio* investigations have addressed their structural and thermodynamic stability in the rocksalt phase^{22,23}. It has been concluded that MnC and FeC are unstable at ambient conditions, but could be stabilized under high pressure or temperature. Interestingly, an unconventional superconductivity was also predicted in MnC²³. A similar study has demonstrated that MnC

would be more stable in hexagonal wurtzite structure²⁴.

According to the calculated formation enthalpies of the manganese-carbon system, the stoichiometric MnC formation is highly unfavorable²⁵. Recently, however, a first successful synthesis was achieved under high-pressure and high-temperature conditions²⁶. The compound was found to be a metal adopting the fourfold coordinated zincblende (ZB) structure, with a lattice constant of 4.429 Å, and suggested as a potential superhard material. However, no data have been provided about its magnetic properties. This experimental achievement presents a theoretical puzzle, since recent calculations concluded that under pressure, MnC would be stable in the rocksalt structure²³. Moreover, early theoretical investigations predicted zincblende MnC as half-metallic ferromagnet with an unusual coexistence of localized and itinerant magnetic moments^{27–29}. This property (e.g. full spin polarization at Fermi level) is highly desirable for spintronic applications^{30,31}.

This raises a fundamental question about the accurate first-principles framework to simultaneously describe the structural stability, electronic, and magnetic properties of MnC. The answer is non-trivial, as it requires a method capable to capture correctly the interplay between covalent Mn–C bonding, electronic correlations, and exchange interactions.

Motivated by these developments, we present a comprehensive DFT study of MnC. We employ a hierarchy of exchange–correlation functionals, ranging from semilocal GGA and meta-GGA to range-separated hybrids and the extended DFT+ U + V approach, with a specific focus on the role of *bond-exchange* interactions. Our goals are threefold: to identify the functional that correctly stabilizes the observed ZB phase, to uncover the physical

mechanism behind this stabilization, and to resolve the conflicting predictions regarding its electronic behavior.

The paper is organized as follows: Sec. II outlines the theoretical methods, where the basics of meta-GGA, hybrid DFT functionals, and the extended DFT+ $U+V$ approach are presented. The computational details are given in Sec. III. The structural stability and the magnetic ordering are discussed in Sec. IV, and we analyze the electronic structure and chemical bonding in Sec. V. To conclude our investigation, we summarize the important results in Sec. VI.

II. THEORY

Although density functional theory (DFT) is, in principle, an exact ground-state theory, the exact form of the exchange-correlation energy functional E_{xc} remains unknown³². Therefore, the practical usage of the Kohn-Sham framework³³ relies entirely on finding suitable approximations, and a panoply of schemes and parameterizations have been developed over time. The classification of the main theoretical advances is nicely illustrated by the Perdew Jacob's ladder³⁴, which ranks functionals by their degree of nonlocality.

A. meta-GGA

The so-called meta-generalized gradient approximations (meta-GGAs) constitute the highest semilocal rung of Jacob's ladder hierarchy avoiding the full non-locality. Like GGAs, they depend on the electron density $n_\sigma(\mathbf{r})$ and its gradient $\nabla n_\sigma(\mathbf{r})$, but they additionally incorporate the positive kinetic-energy density $\tau_\sigma(\mathbf{r})$ ¹, where $\sigma = \{\uparrow, \downarrow\}$ is the spin index³⁴:

$$E_{xc}^{\text{MTGGA}}[n_\sigma] = \int d\mathbf{r} \varepsilon_{xc}^{\text{MTGGA}}(n_\sigma, \nabla n_\sigma, \tau_\sigma) \quad (1)$$

The kinetic-energy densities are constructed from the Kohn-Sham orbitals :

$$\tau_\sigma(\mathbf{r}) = \sum_i^{\text{occ}} \frac{1}{2} |\nabla \phi_i^\sigma(\mathbf{r})|^2 \quad (2)$$

Several parameterizations of the meta-GGA exist in literature, where the well known are the TPSS³⁶, its revised version rev-TPSS³⁷, M06L³⁸ and mBJ³⁹. The recently proposed one, namely the strongly constrained and appropriately normed (SCAN) functional⁴⁰, has attracted much attention. According to the authors, the

most important ingredient making the SCAN superior to previous meta-GGAs, is the dimensionless parameter of the kinetic-energy densities:

$$\alpha = \frac{\tau_\sigma(\mathbf{r}) - \tau_\sigma^{\text{W}}(\mathbf{r})}{\tau_\sigma^{\text{unif}}(\mathbf{r})} > 0, \quad (3)$$

This parameter distinguishes three different bonding characters: covalent ($\alpha = 0$), metallic ($\alpha = 1$) and weak ($\alpha \gg 1$). Many SCAN calculations, on diverse molecular and extended systems, have demonstrated that it leads to very interesting results; especially for structural geometry and energetics⁴¹⁻⁴⁵. Moreover, it is argued that SCAN functional could be suitable (at least qualitatively) for the treatment of strong electronic correlations^{46,47}, and the related ground-state symmetry breaking⁴⁸. We notice finally that two revised formulation of the SCAN functional, known as rSCAN⁴⁹ and r2SCAN⁵⁰, have been recently proposed.

B. Hybrid (Hartree-Fock)-DFT

An outstanding improvement, beyond semilocal DFT, is the *hybrid* functionals. The basic idea, initially proposed by Becke^{51,52}, is to incorporate a fraction of non-local exact exchange from Hartree-Fock (HF) theory into the semi-local E_{xc} . He suggested a simple linear combination:

$$E_{xc}^{\text{Hybrid}} = E_{xc}^{\text{GGA}} + \alpha (E_x^{\text{HF}} - E_x^{\text{GGA}}) \quad (4)$$

where α is obtained by some fitting to the atomization energies. A later improved version, the B3LYP functional⁵³, has become very popular in quantum chemistry community. A next step is the PBE0, described as a parameter-free functional⁵⁴. Based on GGA-PBE⁵⁵, it is derived from equation 4 with a predefined fraction ($\alpha = \frac{1}{4}$), justified by a general analysis from perturbation theory⁵⁶:

$$E_{xc}^{\text{PBE0}} = E_{xc}^{\text{PBE}} + \frac{1}{4} (E_x^{\text{HF}} - E_x^{\text{PBE}}) \quad (5)$$

While the previous functionals belong to the family of *global* hybrid functionals, an important advance is the so-called *range-separated* hybrid functionals, using a *screened* interaction instead of the bare Coulomb potential^{57,58}. In extended systems, this idea is very appealing not only technically but also physically. A *screened* interaction makes the HF exchange more tractable, and accounts for the screening phenomenon established by the random-phase approximation^{59,60}.

In HSE hybrid functionals^{57,58}, the separation (and the screening as a result) is achieved by an error function decomposing the bare Coulomb potential into a short-range (SR) and a long-range (LR) parts:

¹ Notice that in addition, the Laplacians of the electron densities $\nabla^2 n_\sigma(\mathbf{r})$, can be incorporated into the meta-GGA functionals³⁵

$$\frac{1}{r} = \underbrace{\frac{1 - \text{erf}(\omega r)}{r}}_{\text{SR}} + \underbrace{\frac{\text{erf}(\omega r)}{r}}_{\text{LR}} \quad (6)$$

where ω is an adjustable screening parameter⁶¹. The HSE exchange-correlation functional is expressed as:

$$E_{\text{xc}}^{\text{HSE}} = \frac{1}{4}E_{\text{x}}^{\text{HF-SR}} + \frac{3}{4}E_{\text{x}}^{\text{PBE-SR}} + E_{\text{x}}^{\text{PBE-LR}} + E_{\text{c}}^{\text{PBE}} \quad (7)$$

In fact, GGA-PBE and PBE0 hybrid functional are merely restored, from the two particular values $\omega = \infty$ and $\omega = 0$, respectively. In equation 7, only the first term needs to be calculated exactly, and all the remaining ones are computed at the PBE level. Even with this simplification, the HF exact exchange is computationally very expensive. With the Kohn-Sham orbitals $\phi_{n,\mathbf{k}}(\mathbf{r})$, it is defined as:

$$E_{\text{x}}^{\text{HF-SR}} = -\frac{1}{2} \sum_{\sigma} \sum_{n,\mathbf{k}} \sum_{n',\mathbf{k}'} \int \int d\mathbf{r} d\mathbf{r}' (1 - \text{erf}(\omega|\mathbf{r} - \mathbf{r}'|)) \times \frac{\phi_{n,\mathbf{k}}^{\sigma*}(\mathbf{r}) \phi_{n',\mathbf{k}'}^{\sigma}(\mathbf{r}) \phi_{n',\mathbf{k}'}^{\sigma*}(\mathbf{r}') \phi_{n,\mathbf{k}}^{\sigma}(\mathbf{r}')}{|\mathbf{r} - \mathbf{r}'|} \quad (8)$$

Another progress in this field is the recently invented PBE0r hybrid functional⁶², following a new and different approach. The Kohn-Sham orbitals are expanded in a minimal basis of localized atom-centered tight-binding orbitals, allowing a natural decomposition of the HF exchange into:

- *On-site* exchange which acting between states centered on the same atom. It affects the degenerate states and split them into filled and empty bands (the Mott-Hubbard separation in the narrow and partially filled d and f atomic shells).
- *Bond-exchange* describing the intersite exchange between electron densities located at neighboring atoms involved in chemical bonds.
- *Long-range* exchange acting over distances longer than bond lengths. The neglect of this term is indeed advantageous, since the unphysical behavior in metallic solids (due to the long-range tail of the Coulomb interaction) is avoided and the screening is effectively taken into account.

The *bond exchange* term is particularly relevant for covalent materials, as it differentiates between bonding and antibonding states. It mainly corrects the semilocal functionals errors in formation-energy and band gaps.

The use of localized atom-centered orbitals (a natural cutoff of the exchange interaction) and the neglect of the long-range terms (capturing the important screening effects) make PBE0r a *de facto* range-separated functional. Its *local* (i.e. on-site) formulation is defined as:

$$E_{\text{xc}}^{\text{PBE0r}} = E_{\text{xc}}^{\text{PBE}} + \sum_{n=1}^N a_n (E_{x,n}^{\text{HF-onsite}} - E_{x,n}^{\text{PBE-onsite}}) \quad (9)$$

The sum runs over the N atoms of the system (i.e. the cell used in calculations), where a_n represents the mixing factor (fraction) of the HF exact exchange. This formulation is very flexible, since the mixing factor a_n can be set differently for the atomic species; and allows an explicit control of the bond-exchange contribution.

Finally, the accuracy of PBE0r versus experiments has been established for a large variety of systems; such as partially filled d -shell oxides⁶³, transition metal sulfides and nitrides^{30,64,65}, manganese oxide^{66,67}, and iron spin-crossover complexes⁶⁸.

C. Hubbard corrected DFT

In this section, we summarize the basic notions of the Hubbard-corrected DFT methods. We concentrate on the recently proposed DFT+ U + V formalism⁶⁹ (based on the extended Hubbard model), from which the widely used DFT+ U ⁷⁰⁻⁷² can be straightforwardly derived. Starting from any local or semi-local functional, the corresponding DFT+ U + V one is written as:

$$E_{\text{xc}}^{\text{DFT}+U+V} = E_{\text{xc}}^{\text{DFT}} + E_{\text{xc}}^{U+V} \quad (10)$$

Following the definition and the notation adopted in references^{69,73}, the Hubbard correction to the exchange-correlation energy (in the simplified rotationally-invariant formulation) is given by:

$$E_{\text{xc}}^{U+V} = \frac{1}{2} \sum_I \sum_{\sigma mm'} U^I (\delta_{mm'} - n_{mm'}^{II\sigma}) n_{m'm}^{II\sigma} - \frac{1}{2} \sum_I \sum_{J \neq I} \sum_{\sigma mm'} V^{IJ} n_{mm'}^{IJ\sigma} n_{m'm}^{JI\sigma} \quad (11)$$

where U^I and V^{IJ} are, respectively, the on-site and the intersite Hubbard parameters; and the indices I and J run over all the atomic sites. Notice that the sum over J in the second line, covers the all neighboring atoms included in the intersite correction.

In equation 11, the onsite occupation matrix elements $n_{mm'}^{II\sigma}$ are obtained by the projection of the Kohn-Sham states $|\psi_{\mathbf{k}\nu}^{\sigma}\rangle$ on a set of localized (atomic) orbitals $|\phi_m^I\rangle$.

$$n_{mm'}^{IJ\sigma} = \sum_{\mathbf{k}\nu} f_{\mathbf{k}\nu}^{\sigma} \langle \psi_{\mathbf{k}\nu}^{\sigma} | \phi_{m'}^J \rangle \langle \phi_m^I | \psi_{\mathbf{k}\nu}^{\sigma} \rangle \quad (12)$$

where $f_{\mathbf{k}\nu}^{\sigma}$ represent the occupations of the Kohn-Sham states, ν is the electronic band index and \mathbf{k} is the Bloch wave vector. The m (m') index is the magnetic quantum

number, running over the orbital momentum in atom I (J). Notice that the on-site occupation elements $n_{mm'}^{II\sigma}$ can be obtained as a particular case ($I = J$).

At this point, it is important to mention the issue about the values of U and V parameters. These latter are actually unknown, and they are usually tuned by hand to reproduce some experimental data (like lattice constants, magnetic moments and more importantly band gaps). Such a procedure, however, makes DFT+ U + V a partially empirical method. In fact, there exist several first-principles techniques to compute the correct values of U and V . Some of the well known are the constrained DFT (cDFT)^{74–76} and the constrained random-phase approximation (cRPA)^{77–79}. A recent one, using density-functional perturbation theory (DFPT)^{80,81}, has been developed with the main advantage of a significant reduction in the computational cost.

Last but not least, these Hubbard parameters depend intimately on the chemical environment from which they are computed. Thus, they are not transferables i.e. not universal for a given atomic species⁸². In addition, they depend on the kind of the used projector functions^{83,84}.

III. COMPUTATIONAL DETAILS

All calculations were performed within DFT^{32,33}, using three different exchange-correlation schemes. The semi-local framework (GGA-PBESol⁸⁵ and SCAN meta-GGA⁴⁰), Two range-separated hybrid functionals (HSE06⁵⁸ and PBE0r⁶²) and the mean-field DFT+ U + V approach⁶⁹. In the latter, the double counting correction is accounted using the *fully localized limit* formula^{71,86–88}.

The PBESol, SCAN, HSE06 and DFT+ U + V calculations were carried out using the Quantum ESPRESSO package (QE, version 7.1)^{89–91}. In the PBESol, HSE06 and DFT+ U + V , the Kohn-Sham single-particle equations were solved within the projector-augmented wave (PAW) method⁹², using PAW potentials from the PSlibrary⁹³. For SCAN meta-GGA, however, norm-conserving pseudopotentials from the PseudoDojo library⁹⁴ were employed.

Based on density-functional perturbation theory (DFPT), within the linear-response formalism; the on-site U and intersite V parameters were calculated self-consistently using the HP code⁹⁵ (distributed within the QE package). The Γ -centered \mathbf{q} -point mesh was increased up to $3 \times 3 \times 3$ to ensure convergence. Orthogonalized atomic orbitals, obtained via Löwdin method^{83,95,96}, were used as Hubbard projectors functions. Since U and V are not transferables, they were computed separately for the rocksalt and zincblende structures, at each step of the total-energy versus volume optimization.

All calculations were converged with a plane-wave kinetic-energy cutoff of 50 Ry, with a total-energy threshold of 10^{-8} Ry in the self-consistent cycle. The Brillouin zone was sampled following the Monkhorst-Pack

scheme⁹⁷, using a $18 \times 18 \times 18$ mesh (200 \mathbf{k} -point). For metallic states, the electronic smearing was treated using the Marzari-Vanderbilt scheme⁹⁸, with a broadening parameter of 0.02 Ry. The calculations of the electronic densities of states, however, were carried out with the improved linear tetrahedron method⁹⁹.

The PBE0r hybrid functional calculations were performed using the PAW method⁹², within its original implementation provided in the CP-PAW code¹⁰⁰. We recall that PAW is by construction an *all-electron* method, using augmented-waves. The included orbitals in the PAW augmentation are: $2s$, $2p$, and $3d$ of C, and $3s$, $3p$, $3d$, $4s$, and $4p$ of Mn; with covalent radii of 0.71 Å (C) and 1.17 Å (Mn). In addition, Mn $3s$ and $3p$ semi-core states were treated as valence orbitals. As mentioned above in section II B, PBE0r uses a localized tight-binding orbitals basis, including the $2s$ and $2p$ orbitals of C, and the $3s$, $3p$, $3d$, and $4s$ ones of Mn.

The CP-PAW code uses the Car-Parrinello *ab initio* molecular dynamics (AIMD)¹⁰¹, where the ground-state is reached by applying a friction term (a damped MD). Here also, and to be in line with QE calculations, a plane-wave kinetic-energy cutoff of 50 Ry for the auxiliary wave functions was used. The total energy was minimized up to a convergence threshold of 10^{-5} Hartree, and the improved linear tetrahedron method⁹⁹ was used for the Brillouin zone integration (with 200 \mathbf{k} -points). To deal with fractional occupations in metallic systems, the Mermin functional¹⁰² was used.

A significant advantage of PBE0r functional is its low computational cost, that is comparable to GGA^{66,67}. In the present study, the same value of the mixing factor is assigned for both C and Mn atoms. As mentioned above (section II B), however, HSE06 calculations are extremely expensive; especially with plane-waves⁷³. To assess the exact exchange effect on MnC properties, we have used two fractions of the exact exchange: 10% and 30%, with a $3 \times 3 \times 3$ uniform \mathbf{q} -point mesh.

IV. GROUND-STATE CRYSTAL STRUCTURE AND MAGNETIC ORDER

Structural stability of MnC is investigated in the two faces-centered cubic: rocksalt (RS) and zincblende (ZB) structures. This choice is motivated by the fact that all known monoxides, mononitrides and monocarbides are found to crystallize in either of these two prototypes. For each structure, both spin-polarized ferromagnetic (FM) and type-II antiferromagnetic (AF-II) are considered. In the latter, ferromagnetic planes alternate along the $\langle 111 \rangle$ direction, as commonly observed in MnO and NiO.

As an aside note, additional calculations for MnC in the wurtzite structure have been performed. It was found to be the most unstable phase and the corresponding results are therefore omitted.

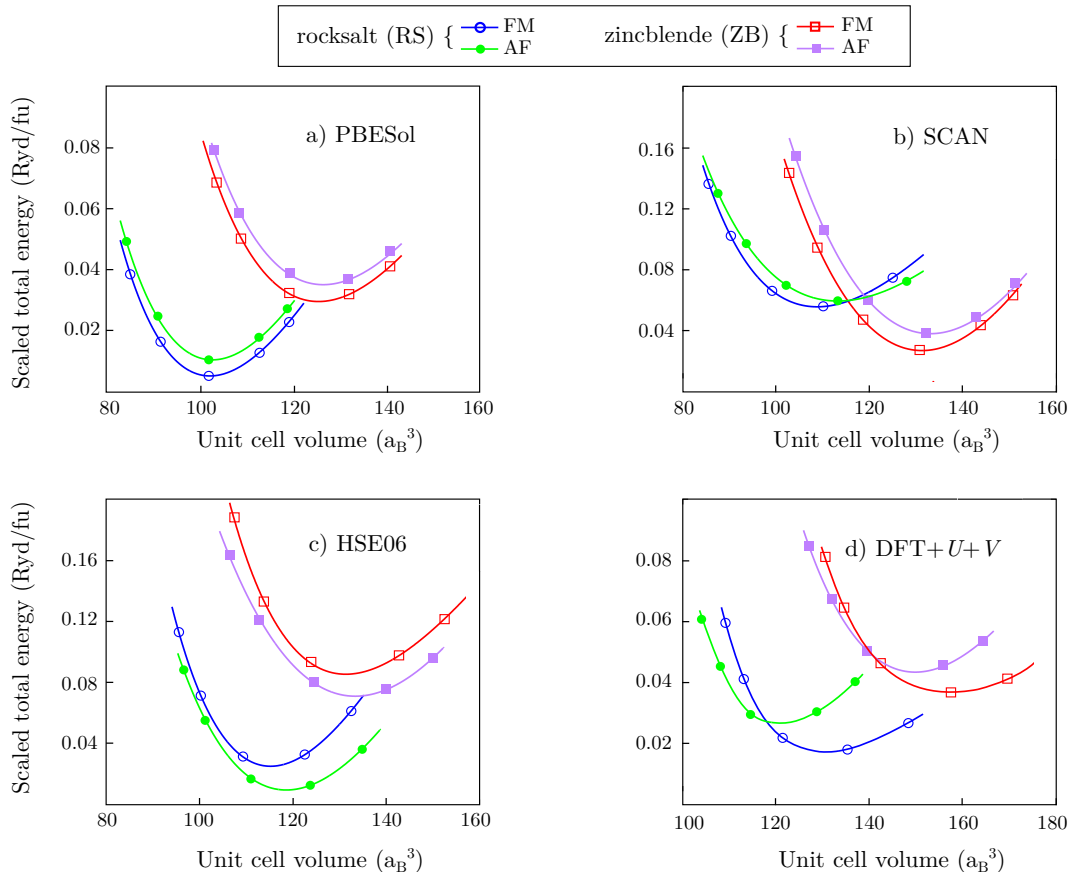


FIG. 1: Energy versus volume optimization of MnC in rocksalt (RS) and zincblende (ZB) structures; as obtained within QE: a) PBESol, b) SCAN, c) HSE06 and d) DFT+ $U+V$ functionals.

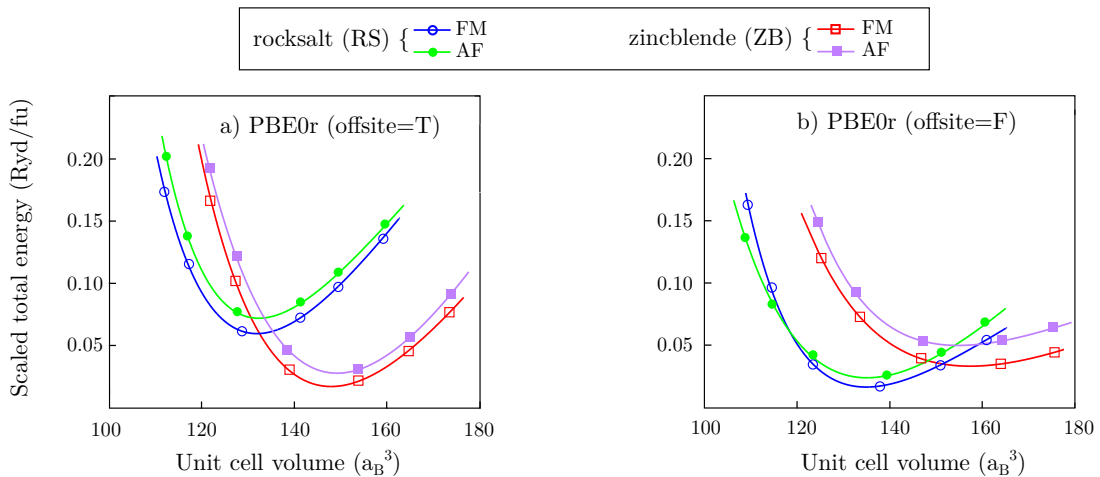


FIG. 2: Energy versus volume optimization of MnC in rocksalt (RS) and zincblende (ZB) structures; as obtained within PBE0r functional: a) PBE0r (offsite=T) with the bond exchange, and b) PBE0r (offsite=F) without the bond exchange.

A. Structural stability

Theoretical ground-state is obtained from the energy versus volume optimization. The results from PBESol, SCAN, HSE06 and DFT+ $U+V$ are shown in Fig. 1, and

those from PBE0r (with and without the inclusion of *bond exchange*) are presented in Fig. 2. The curves were fitted with the third-order of Birch-Murnaghan equation of state¹⁰³. The important finding is that SCAN and PBE0r successfully reproduce the experimentally ob-

TABLE I: Calculated total energies differences (in Ryd/fu) between FM and AF-II orders in the rocksalt (RS) and zincblende (ZB) structures, and between the two phases at theoretical equilibrium; as arising from all the frameworks.

	$E_{\text{FM}} - E_{\text{AF-II}}$		$E_{\text{RS}} - E_{\text{ZB}}$
	RS	ZB	
PBESol	- 0.003	- 0.005	- 0.028
SCAN	- 0.006	- 0.008	+ 0.035
PBE0r	- 0.015	- 0.010	+ 0.043
HSE06	+ 0.020	+ 0.015	- 0.045
DFT+ $U+V$	- 0.008	- 0.005	- 0.029

served zincblende ground state structure, while the others incorrectly stabilize the rocksalt one. The computed total-energy differences at equilibrium are provided in Tab. I. It is important to mention that for PBE0r, only a 10% fraction of exact exchange was sufficient to reproduce the correct structure, whereas with a fraction as high as 30% HSE06 still predict a stable rocksalt phase.

The failure of the GGA-type functionals is actually not new, and has been reported in several other cases, such as MnN compound^{10,14,107}. In that case, however, hybrid functionals and GGA+ U approaches were able to remedy this issue¹². Interestingly, neither the usually accurate HSE06 nor the DFT+ $U+V$ method are able to predict the correct MnC structure.

B. Role of bond exchange

This result can be addressed using the flexibility of PBE0r framework, where two kinds calculations are shown in Fig. 2:

- a) with *bond*-exchange included (offsite=T, that refers to the exchange interaction offsite terms)
- b) with only on-site exchange (offsite=F)

The PBE0r results provide explicit evidence of the importance of the *bond*-exchange term in stabilizing the ZB phase. When it is ignored, the rocksalt phase becomes energetically favored. This exchange term has the characteristic to distinguish between bonding and antibonding states, and acts differently on their occupations. As a result, it accounts better for the covalency effects and reduce the formation energy errors. To assess quantitatively this contribution in each phase, the total energy difference $\Delta E = E_{(\text{offsite}=\text{T})} - E_{(\text{offsite}=\text{F})}$ is provided: $\Delta E_{\text{RS}} = -0.196$ Ryd and $\Delta E_{\text{ZB}} = -0.311$ Ryd. This shows clearly that neglecting the *bond*-exchange contribution introduces a much larger error in the zincblende structure than in the rocksalt one.

Concerning SCAN functional, its main advantage is the ability to recognize different types of bonding. From a benchmark calculations (up to 1000 compounds known experimentally), it was found that the formation energy errors in covalent systems decrease substantially (by \sim

50% compared to GGA-PBE). The reason behind this success is the enhanced exchange interaction in the covalent regime^{39,43}. This agreement between SCAN and PBE0r indicates that the enhanced exchange interaction built into SCAN plays a role analogous to the explicit *bond*-exchange in PBE0r.

Both frameworks highlight the important role of covalent exchange effects in MnC. In fact, the Mn-C bond involves significant hybridization between Mn-3*d* and C-2*p* orbitals; thus, conventional GGAs treating exchange isotropically underestimate the energy gain associated with covalent bonding. The explicit inclusion of this term (PBE0r) or its implicit treatment via the kinetic-energy density parameter (SCAN) both strengthen Mn-C hybridization. These findings emphasize that accurate treatment of bond-directional exchange is crucial for describing structural stability in late 3*d* transition-metal carbides, where the interplay between metallic and covalent bonding is not clear cut.

We believe that the inability of HSE06 and DFT+ $U+V$ to capture this stabilization can be attributed to the absence of such bond-selective exchange. HSE06 mixes a whole and fixed fraction of exact exchange into the GGA functional without differentiating bonding and antibonding contributions. The same argument hold as well for the DFT+ $U+V$ method. Despite the existence of V intersite parameter; it cannot fully capture the Mn-C covalency.

C. Equilibrium Properties and Magnetic Ordering

The equilibrium values of lattice constants (in Å), bulk moduli (in GPa) and magnetic moments per formula unit M_{fu} (in μ_{B}) obtained from each framework are summarized in Tab. II; along with available theoretical and experimental data.

Compared to the only available experimental lattice constant of zincblende MnC²⁶, semilocal PBESol and SCAN functionals tend to underestimate it, while DFT+ $U+V$ overestimates it. On the other side, the hybrid functionals yield a close agreement with experiment. In particular the PBE0r result of 4.44 Å is almost perfect. To our knowledge, MnC has not been elaborated in the rocksalt structure, and our PBESol results agree very well with previous GGA calculations^{23,24}. The bulk moduli follow an opposite trend: semilocal functionals agree better with experimental results, whereas hybrid and DFT+ $U+V$ schemes yield stiffer or softer lattices, respectively.

Total energies differences between the FM and AF-II states, in both crystal structures are provided in Tab. I. The FM order is energetically favored over the AF-II configuration in all frameworks, except in HSE06 where the opposite is predicted. The computed magnetic moments per formula unit reveal clear functional-dependent trends, with larger values in the RS phase. While PBESol and SCAN yield smaller moment, hybrid functionals

TABLE II: Calculated equilibrium properties within all the used frameworks, for MnC in rocksalt (RS) and zincblende (ZB) structures. The lattice constant a in Å, the magnetic moment per formula unit M_{fu} in μ_B (in the FM case) and the bulk modulus B in GPa are shown.

	RS			ZB		
	a	B	M_{fu}	a	B	M_{fu}
<u>PBESol</u>						
FM	3.97	230	1.15	4.22	172	1.00
AF	3.98	232		4.23	166	
<u>SCAN</u>						
FM	4.02	224	1.30	4.28	175	1.00
AF	4.08	219		4.31	169	
<u>PBE0r</u>						
FM	4.15	214	2.88	4.44	192	2.05
AF	4.17	210		4.48	150	
<u>HSE06</u>						
FM	4.10	238	2.58	4.32	201	1.94
AF	4.14	220		4.35	189	
<u>DFT+U+V</u>						
FM	4.27	211	3.04	4.51	116	3.00
AF	4.17	204		4.46	102	
<u>Theory</u>						
Ref. ²⁴	4.02	295		4.31	240	
Ref. ²⁷				4.23		
Ref. ²⁹				4.20		
<u>Experimental</u>						
Ref. ²⁶				4.43	170	

(HSE06 and PBE0r) enhance the exchange splitting and produce larger values. Finally, the DFT+ $U+V$ method yields the largest moments, reflecting a stronger on-site exchange interactions.

The integer magnetic moments obtained within semilocal and DFT+ $U+V$ frameworks suggest a half-metallic nature for ZB–MnC. This prediction is examined in more detail in the following section.

V. ELECTRONIC STRUCTURE AND BONDING PROPERTIES

In this section, we analyze the electronic structure and chemical bonding properties of MnC in both rocksalt (RS) and zincblende (ZB) phases. The results are presented in terms of the site-, orbital-, and spin-projected densities of states (PDOS), as computed within the various exchange–correlation frameworks discussed above. To elucidate the crystal field effects, the Mn 3*d*-states are splitted into Mn- t_{2g} and Mn- e_g manifolds, corresponding to octahedral and tetrahedral coordination, respectively. In addition, we concentrate on the ground state spin-polarized ferromagnetic configuration; where a particular attention is paid to the nature of half-metallic ferromagnetism and to how the choice of functional affects the Mn–C bonding and spin polarization.

A. Semi-local PBESol and SCAN

First, the MnC electronic structure is explored within PBESol functional, where the obtained densities of states are shown in Fig. 3. In general, there are three main regions corresponding to bonding, non-bonding and anti-bonding states.

For the rocksalt structure (the upper panel of Fig. 3), the bonding region [−8 eV, −3 eV] is formed by Mn- e_g and C- p hybridized states with a strong σ -type overlap characteristic of the octahedral arrangement. Next, the non-bonding part dominated by the Mn- t_{2g} manifold from −3 eV to +1 eV. In the remaining higher energy window, the Mn- e_g and C- p hybridization forms the anti-bonding counter-part. The RS phase has clearly a metallic behavior, and the small exchange splitting indicates a low-spin configuration; with a magnetic moment value of $\sim 1.15 \mu_B$ arising primarily from the Mn- t_{2g} states.

In the zincblende structure, the crystal-field splitting is obviously inverted due to the tetrahedral environment, such that the Mn- t_{2g} orbitals form the bonding manifold. As displayed in Fig. 3 (the lower panel), the bonding region [−6 eV, −3 eV] contains hybridized Mn- t_{2g} and C- p states. The non-bonding region is dominated by two Mn- e_g bands (one occupied and one empty), still with a small contribution of Mn- t_{2g} . Above +1.5 eV, the anti-bonding region contains essentially C- p and Mn- t_{2g} hybrid states. The large separation between bonding and anti-bonding parts of the Mn- t_{2g} manifold indicates the high strength of the Mn–C bond. More importantly, zincblende MnC

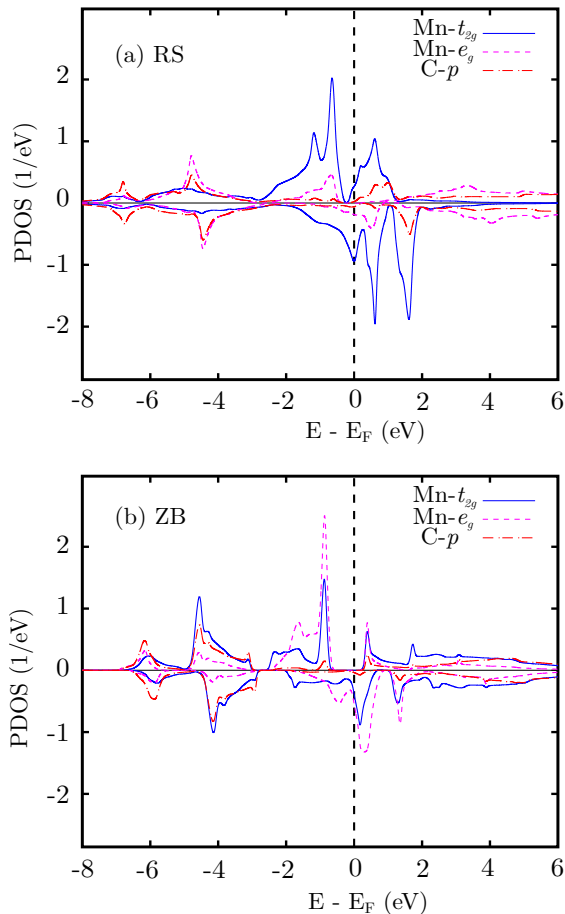


FIG. 3: Atom- and spin-resolved densities of states (PDOS) of MnC in RS-type (a) and ZB-type (b) structures, as arising from the PBESol spin-polarized FM calculations.

is insulating in the majority-spin channel with an energy gap of about 1.2 eV, while being metallic in the minority-spin one. This yields a half-metallic ferromagnet with 1 μ_B magnetic moment (from the occupied Mn- e_g band), consistent with previous predictions^{27–29}.

Although SCAN predicts the correct ZB ground state, its electronic PDOS spectra are very similar to those of PBESol (see Fig. 4). In fact, it has been already pointed out that meta-GGAs (including SCAN) do not really improve over GGA for electronic and magnetic properties (band gaps, magnetic moments)^{43,45,47}.

Within SCAN framework, MnC is also predicted as a ferromagnetic metal in rocksalt structure and a ferromagnetic half-metal in zincblende one. The whole distribution of the bonding, non-bonding and anti-bonding regions is almost the identical to PBESol. The only noticeable difference is that the Fermi level is slightly pushed upward at the vicinity of a non-vanishing DOS, placing the compound near a fully metallic state. Such sensitivity to the lattice constant (here SCAN: 4.28Å versus PBESol: 4.22Å) has been mentioned previously, where a small increase drives zincblende MnC from half-metallic to metallic state^{27,28}.

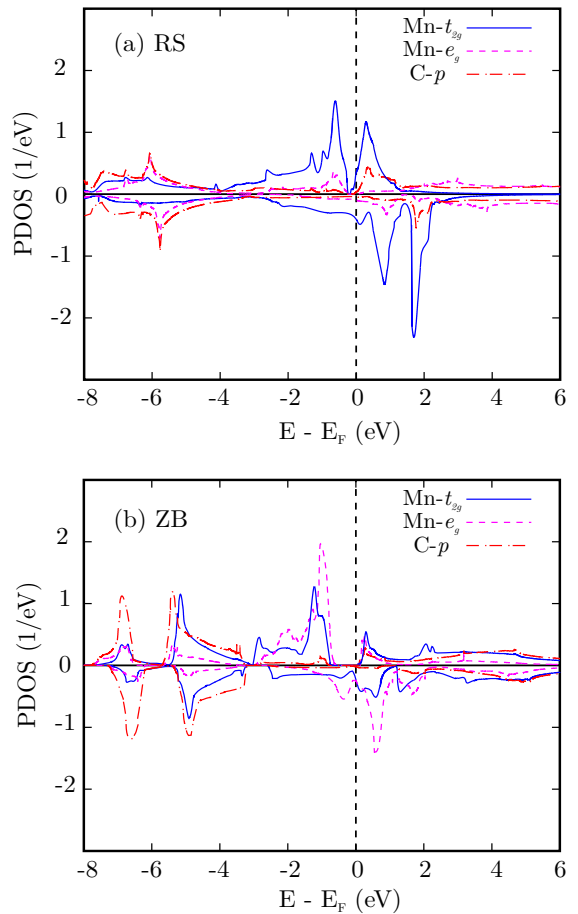


FIG. 4: Atom- and spin resolved densities of states (PDOS) of MnC in RS-type (a) and ZB-type (b) structures, as arising from the SCAN spin-polarized FM calculations.

B. Hybrid PBE0r and HSE06

To assess the effect of a partial inclusion of the non-local HF exchange; we used PBE0r and HSE06 hybrid functionals, with two different fractions 10% and 30%. In each crystalline phase, both fractions yield typically similar trends in the electronic PDOS (bonding, non-bonding and anti-bonding regions). The only difference is the stronger exchange splitting with the larger fraction, producing larger magnetic moments. The electronic PDOS obtained from PBE0r and HSE06 are displayed in Fig. 5 and Fig. 6, respectively. As a first results, the two functionals lead to a metallic MnC in both RS and ZB structures.

In the rocksalt phase, the inclusion of exact exchange substantially enhances the spin splitting of the Mn-3d states, especially for the non-bonding Mn- t_{2g} ones. In PBE0r, the corresponding shift is more pronounced, so that the majority (minority) spin states are almost filled (empty). This drives the Mn- t_{2g} manifold (three-fold degenerate) to a quasi high-spin configuration, whereby the value of the magnetic moment $\simeq 3 \mu_B$ (see Tab. II). In

HSE06, a similar situation is found but with a slightly less important splitting.

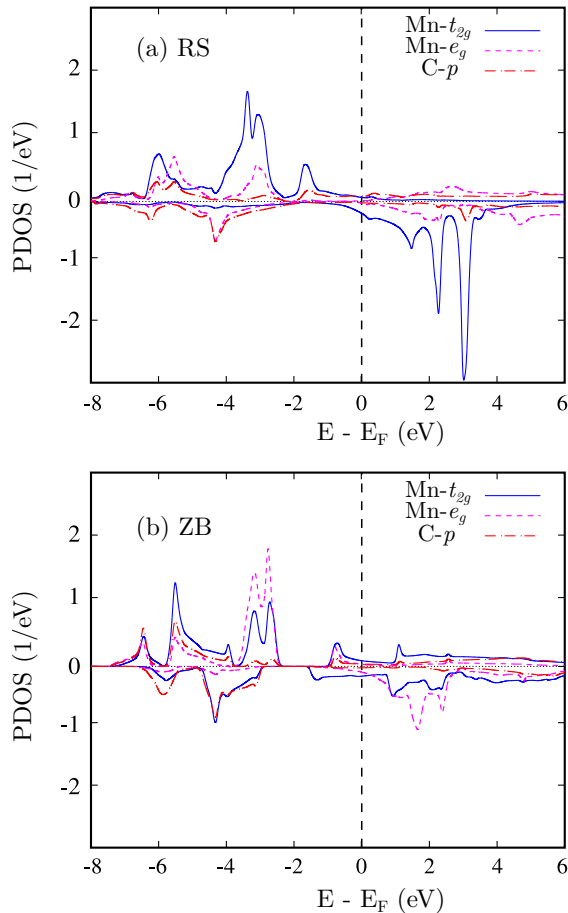


FIG. 5: Atom- and spin resolved densities of states (PDOS) of MnC in RS-type (a) and ZB-type (b) structures, as arising from the PBE0r, with *bond* exchange (offsite=T), spin-polarized FM calculations.

In the zincblende structure, the same description holds for the two hybrid functionals. The Mn- e_g manifold (two-fold degenerate) experience the largest exchange splitting driving it toward a high-spin configuration, consistently with the computed magnetic moments. However, in contrast to the semilocal functionals, both hybrid PBE0r and HSE06 predict a fully metallic ZB-MnC at theoretical equilibrium. The disappearance of the half-metallicity is primarily due to lattice expansion, since both hybrid functionals yield larger equilibrium volumes (see Tab. II); in complete agreement with GGA predictions.

To confirm this result, additional PBE0r and HSE06 calculations have been carried out; at smaller lattice constants, as obtained from PBESol and SCAN. The obtained results (not shown here), indicate that the majority-spin gap reappears and the half-metallicity is restored. Thus, all functionals agree that ZB-MnC is a half-metal at reduced volumes (≤ 4.3 Å); and becomes metallic under expansion. Consequently, the compound is expected to behave as a ferromagnetic metal at the

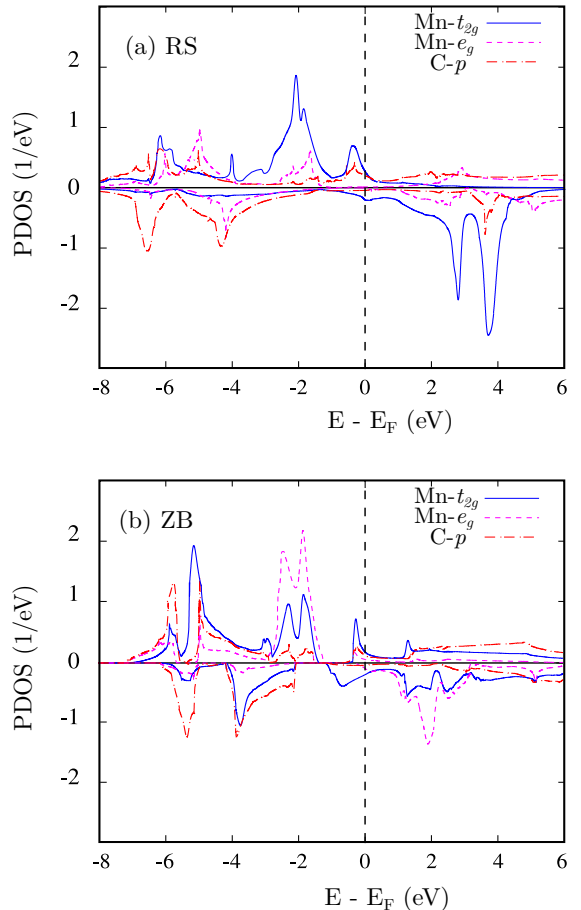


FIG. 6: Atom- and spin resolved densities of states (PDOS) of MnC in RS-type (a) and ZB-type (b) structures, as arising from the HSE06 spin-polarized FM calculations.

experimental lattice constant (~ 4.4 Å).

C. Mean field DFT+ U + V

TABLE III: The calculated values of the onsite U and the intersite V Hubbard parameters for Mn 3d states, in eV, at: DFT+ U + V and PBESol lattice constants; as well as the experimental one. The values are for ferromagnetic solution only; in the rocksalt (RS) and zincblende (ZB) structures.

		RS	ZB
a DFT+ U + V	U	5.60	5.50
	V	0.57	0.70
a PBESol	U	5.93	5.85
	V	0.64	0.81
a Exp.	U		5.53
	V		0.76

The DFT+ U + V framework offers a complementary picture by explicitly introducing on-site U and intersite V Coulomb interactions. These parameters are computed

self-consistently using the linear response DFPT method; and the obtained values at theoretical equilibrium are shown in Tab III. For sake of completeness, we also provide the computed values at the PBESol equilibrium, and at the zincblende experimental lattice constant (4.43 Å). While the on-site U remains nearly constant (5.5–5.9 eV), the intersite term V decreases with increasing lattice constant, reflecting the reduced overlap between neighboring Mn and C orbitals. These values are somewhat smaller than those typically found in transition-metal monoxides (For example, in MnO and NiO the U parameter is larger than 6 eV^{104–106}), confirming the weaker electronic correlations in MnC.

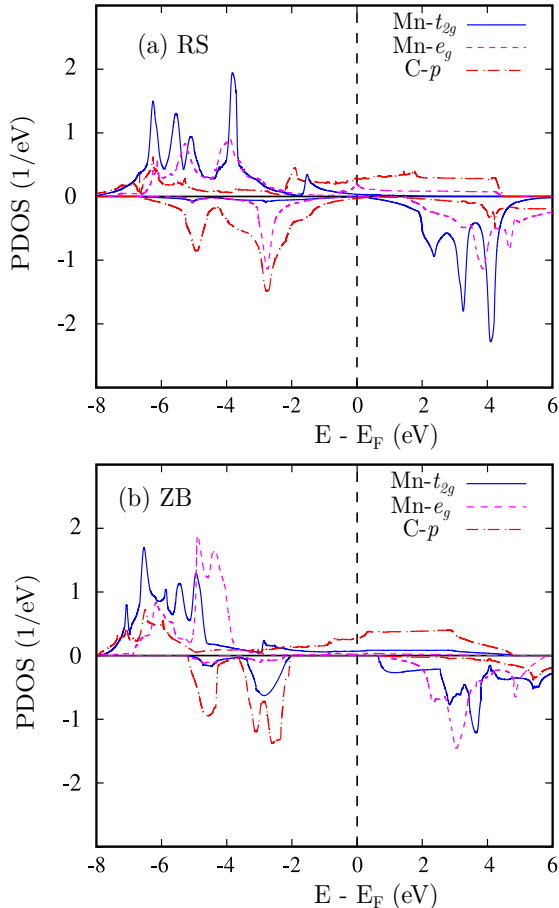


FIG. 7: Atom- and spin resolved densities of states (PDOS) of MnC in RS-type (a) and ZB-type (b) structures, as arising from the DFT+ U + V spin-polarized FM calculations.

The PDOS obtained from DFT+ U + V (shown in Fig. 7) reveals several distinctive features. In the rock-salt phase, the Mn- t_{2g} manifold (three-fold degenerate) is fully polarized i.e. in a complete high-spin configuration, giving rise to the largest computed magnetic moment value ($M_{\text{fu}} \geq 3 \mu_{\text{B}}$).

In the zincblende phase, the system is in a half-metallic state with a moderate minority-spin gap (~ 2.5 eV), in contrast to the predictions of hybrid PBE0r and HSE06. The total moment is $3 \mu_{\text{B}}$, where the high-spin Mn- e_g

manifold contribute with $2 \mu_{\text{B}}$ and the remaining $1 \mu_{\text{B}}$ comes mainly from Mn- t_{2g} states.

Interestingly, while semilocal functionals and DFT+ U + V agree on the half-metallicity, the band gap resides in opposite spin channels. Curiously, in DFT+ U + V this behavior occurs at a lattice constant (4.55 Å) much larger than the limit (≤ 4.30 Å) predicted by semi-local functionals. Additional DFT+ U + V calculations (using the corresponding calculated parameters, see Tab. III) show that the half-metallicity persists at the experimental lattice constant (4.43 Å), and vanishes only under strong compression at the PBESol volume. This opposite volume trend highlights fundamental differences on how semilocal and hybrid functionals in one side, and Hubbard-corrected ones in the other, treat the MnC half-metallic behavior.

In this context, a similar observation has been made for several compounds crystallizing in the zincblende structure. For many pnictides, such as Mn(Cr)As(Sb), GGA calculations predicted a half-metallic behavior with a minority-spin gap, disappearing under compression²⁸. In the same work, MnC was the only half-metal with majority-spin gap.

D. Discussion

Across all theoretical frameworks, the Mn($3d$)-C($2p$) hybridization defines the essential features about the bonding properties and the electronic structure of MnC. Our comprehensive calculations reveal some disagreements on the electronic ground state of ZB-MnC. This is not a failure of the methods but a reflection of the compound's sensitive position at the boundary between a half-metal and a correlated metal. The predictions fall into two distinct categories:

1. Hybrid and semilocal functionals agree that half-metallicity appears at small volume and vanishes upon a slight expansion (~ 4.30 Å). At the experimental lattice constant (~ 4.43 Å), accurately provided by PBE0r, MnC is consistently predicted as a metal. The non-local exact exchange enhances exchange splitting and magnetic moments.

2. On the other side, DFT+ U + V favors half-metallicity at large volume, but with a different nature. It predicts a robust half-metallic state, with a moderate minority-spin gap, persisting at the experimental volume and disappears only under strong compression.

This divergence creates a clear theoretical controversy, where the more structurally accurate hybrid functionals suggest a metal; and methods that often better describe localized states suggest half-metallicity. Such controversy could be resolved by experiment, with specific techniques:

- A direct measurement of the spin polarization at the Fermi level, via spin-resolved photoemission spectroscopy (SPES) or angle-resolved photoemission (ARPES) to confirm Metallic vs. Half-Metallic behavior.

- High-pressure electrical transport and magnetization

measurements could track the volume dependence of the conductivity and magnetic moment.

Therefore, the true electronic ground state of MnC remains an exciting open question, whose resolution will have significant implications for its practical applications.

VI. CONCLUSION

A comprehensive first-principles investigation of MnC properties was carried out, using the state-of-the-art of DFT based methods: PBESol, SCAN, hybrid functionals (PBE0r and HSE06), and the mean field DFT+ U + V . The main goal was to identify the origin of the experimentally observed zincblende structure, and to examine the role of bond exchange in its structural stability as well as electronic behavior.

Our results demonstrate that the stabilization of this experimental structure is uniquely achieved by the SCAN meta-GGA and the PBE0r hybrid functional. This success is attributed to the improved (implicit or explicit) treatment of *bond-directional exchange* interactions in covalent systems. The decisive role of this exchange term is quantitatively proven by its explicit inclusion in PBE0r, which selectively stabilizes the tetrahedral ZB phase by favoring bonding over antibonding states. This shows that an accurate orbital-selective treatment of exchange is crucial for describing the structural chemistry of MnC.

Beyond crystal structure, our investigation reveals a fundamental issue in predicting the electronic ground state. While semilocal functionals (PBESol, SCAN) and DFT+ U + V predict integer moments and half-metallicity, albeit in opposite spin channel, hybrid functionals (HSE06, PBE0r) yield larger magnetic moments and metallic state. The electronic character is found to be strongly volume-dependent: semi-local and hybrid functionals point towards a disappearance of the half-metallicity under expansion, but the opposite is observed with the DFT+ U + V approach. This discrepancy highlights the sensitive position of MnC at the boundary between a correlated metal and a half-metal. It establishes the material's electronic state as an open question for both theory and experiment.

Therefore, we conclude that the true ground state of ZB-MnC is best described by a framework that prioritizes bond exchange, such as SCAN or PBE0r. These methods consistently lead to a ferromagnetic metal at ambient synthesis conditions, with a potential transition to a half-metallic state under compression. Taken together, these findings establish MnC as a model system for studying the interplay between covalent bonding and exchange interactions in late $3d$ transition-metal compounds. Finally, this work not only clarifies the properties of a newly synthesized material but also proposes a clear roadmap for its experimental validation.

* corresponding author: abdeslam.houari@univ-bejaia.dz

- ¹ J. H. de Boer and E. J. W. Verwey, Proc. Phys. Soc. **49**, 59 (1937).
- ² N. F. Mott and R. Peierls, Proc. Phys. Soc. **49**, 72 (1937).
- ³ A. Fujimori and F. Minami, Phys. Rev. B **30**, 957 (1984).
- ⁴ A. Fujimori, K. Terakura, M. Taniguchi, S. Ogawa, S. Suga, M. Matoba, and S. Anzai, Phys. Rev. B **37**, 3109 (1988).
- ⁵ G. A. Sawatzky and J. W. Allen, Phys. Rev. Lett. **53**, 2339 (1984).
- ⁶ J. Zaanen, G. A. Sawatzky, and J. W. Allen, Phys. Rev. Lett. **55**, 418 (1985).
- ⁷ A. Leineweber, R. Niewa, H. Jacobs, and W. Kockelmann, J. Mater. Chem. **10**, 2827 (2000).
- ⁸ K. Suzuki, H. Morita, T. Kaneko, H. Yoshida, and H. Fujimori, J. Alloys. Compd. **201**, 11 (1993).
- ⁹ K. Suzuki, T. Kaneko, H. Yoshida, Y. Obi, H. Fujimori, and H. Morita, J. Alloys. Compd. **224**, 232 (1995).
- ¹⁰ K. Suzuki, T. Kaneko, H. Yoshida, Y. Obi, H. Fujimori, and H. Morita, J. Alloys Compounds **306**, 66 (2000).
- ¹¹ A. Houari, S. F. Matar, M. Belkhir Comput. mat. science. **43**, 392 (2008)
- ¹² J. A. Chan, J. Z. Liu, H. Raebiger, S. Lany, and A. Zunger, Phys. Rev. B **78**, 184109 (2008).
- ¹³ A. Houari, S. F. Matar, M. Belkhir and M. Nakhil, Phys. Rev. B **75**, 064420 (2007).
- ¹⁴ M. S. Miao and W. R. L. Lambrecht, Phys. Rev. B **76**, 195209 (2007).
- ¹⁵ H. R. Soni, V. Mankad, S. K. Gupta and P. K. Jha, J.

Alloys. Compd. **522**, 106 (2012).

- ¹⁶ H. Wang, and D. S. Xue, Chin. Phys. Lett. **21**, 1612 (2004).
- ¹⁷ C. Paduani, Solid. State. Commun. **148**, 297 (2008).
- ¹⁸ A. Houari, S. F. Matar, and V. Eyert, Electron. Struct. **1** 015002 (2019).
- ¹⁹ D. J. Singh, and B. M. Klein, Phys. Rev. B **46**, 14969 (1992).
- ²⁰ Q. Wang, K. E. German, A. R. Oganov, H. Dong, O. D. Feys, Y. V. Zubavichush and V. Y. Murzinh RSC. Adv. **6**, 16197 (2016).
- ²¹ J. Häglund, A. Fernandez Guillermet, G. Grimvall and M. Korling, Phys. Rev. B **48**, 11685 (1993).
- ²² G. L. Gutsev, L. Andrews, C. W. Bauschlicher, Theor. Chem. Acc. **109**, 298 (2003).
- ²³ N. J. Szymanski, I. Khatri, J. G. Amar, D. Gall and S. V. Khare J. Mater. Chem. C, **7** 12619 (2019).
- ²⁴ I. Khatri, N. J. Szymanski, B. B̄Dumre, J. ḠAmar, D. Gall, S. V̄Khare Journal. Alloys. and Compounds. **891**, 161866 (2022).
- ²⁵ D. Djurovic, B. Hallstedt, J. von Appen, and R. Dronskowski, CALPHAD. Comput. Coupling Phase Diagrams Thermochem. **34**, 279 (2010).
- ²⁶ A. N. A. Aparajita, N. R. S. Kumar, S. Chandra, S. Amirthapandian, N. V. C. Shekar uand K. Sridhar, Inorg. Chem. **57**, 14178, (2018).
- ²⁷ E. Sasioglu, I. Galanakis, L. M. Sandratskii, and P. Bruno J. Phys. : Condens. Matter. **17**, 3915 (2005).
- ²⁸ J. E. Pask, L. H. Yang, C. Y. Fong, W. E. Pickett, and

- S. Dag Phys. Rev. B **67**, 224420 (2003).
- ²⁹ M. C. Qian, C. Y. Fong, and L. H. Yang Phys. Rev. B **70**, 052404 (2004).
- ³⁰ A. Houari and P. E. Blöchl, J. Phys. : Condens. Matter **30**, 305501 (2018).
- ³¹ W. E. Pickett and J. S. Moodera, Phys. Today **54**, 39 (2001).
- ³² P. Hohenberg and W. Kohn, Phys. Rev. **136**, B864 (1964).
- ³³ W. Kohn and L. J. Sham, Phys. Rev. **140**, A1133 (1965).
- ³⁴ J. P. Perdew, K. Burke, and M. Ernzerhof, AIP Conf. Proc. **577**, 1 (2001).
- ³⁵ J. P. Perdew, S. Kurth, A. Zupan and P. Blaha, Phys. Rev. Lett. , **82**, 2544 (1999).
- ³⁶ J. Tao, J. P. Perdew, V. N. Staroverov, and G. E. Scuseria, Phys. Rev. Lett. **91**, 146401 (2003).
- ³⁷ J. P. Perdew, A. Ruzsinszky, G. I. Csonka, L. A. Constantin, and J. Sun, Phys. Rev. Lett. **103**, 026403 (2009).
- ³⁸ Y. Zhao and D. G. Truhlar, J. Chem. Phys. **125**, 194101 (2006).
- ³⁹ F. Tran, P. Blaha, Phys. Rev. Lett. **102**, 226401 (2009).
- ⁴⁰ J. Sun, A. Ruzsinszky, and J. P. Perdew, Phys. Rev. Lett. **115**, 036402 (2015).
- ⁴¹ J. Sun, R. C. Remsing, Y. Zhang, Z. Sun, A. Ruzsinszky, H. Peng, Z. Yang, A. Paul, U. Waghmare, X. Wu, M. L. Klein, and J. P. Perdew, Nat. Chem. **8**, 831 (2016).
- ⁴² Y. Zhang, D. A. Kitchaev, J. Yang, T. Chen, S. T. Dacek, R. A. Samiento-Perez, M. A. L. Marques, H. Peng, G. Ceder, J. P. Perdew, and J. Sun, npj Comput. Mater. **4**, 9 (2018).
- ⁴³ E. B. Isaacs and C. Wolverton, Phys. Rev. Mater. **2**, 063801 (2018).
- ⁴⁴ F. Tran, J. Stelzl, P. Blaha. J. Chem. Phys. **144**, 204120 (2016).
- ⁴⁵ V. Sokolovskiy, D. Baigutlin, O. Miroshkina, V. Buchelnikov, Metals. **13**, 728 (2023).
- ⁴⁶ C. Lane, J. W. Furness, I. G. Buda, Y. Zhang, R. S. Markiewicz, B. Barbiellini, J. Sun, and A. Bansil, Phys. Rev. B **98**, 125140 (2018).
- ⁴⁷ Y. Fu and D. Singh, Phys. Rev. B **100**, 045126 (2019).
- ⁴⁸ J. P. Perdew, A. Ruzsinszky, J. Sun, N. K. Nepal, and A. D. Kaplan, P. N. A. S. *118*, e20178501118 (2021).
- ⁴⁹ A. P. Bartok, and J. R. Yates, J. Chem. Phys. **150**, 161101 (2019).
- ⁵⁰ J. W. Furness, A. D. Kaplan, J. Ning, J. P. Perdew, and J. Sun, J. Phys. Chem. Lett. **11**, 8208 (2020).
- ⁵¹ A. D. J. Becke, Chem. Phys. **98**, 1372 (1993).
- ⁵² A. D. J. Becke, Chem. Phys. **98**, 5648 (1993).
- ⁵³ P. J. Stephens, F. J. Devlin, C. F. Chabalowski, and M. J. Frisch, J. Phys. Chem. **98**, 11623 (1994)
- ⁵⁴ C. Adamo and V. Barone, J. Chem. Phys. **110**, 6158 (1999).
- ⁵⁵ J. P. Perdew, K. Burke, and M. Ernzerhof, Phys. Rev. Lett. **77**, 3865 (1996); Phys. Rev. Lett. **78**, 1396(E) (1997).
- ⁵⁶ J. P. Perdew, M. Ernzerhof, and K. Burke, J. Chem. Phys. **105**, 9982 (1996).
- ⁵⁷ J. Heyd, G. E. Scuseria, and M. Ernzerhof J. Chem. Phys. **118**, 8207 (2003).
- ⁵⁸ J. Heyd, G. E. Scuseria, and M. Ernzerhof J. Chem. Phys. **124**, 219906 (2006).
- ⁵⁹ D. Bohm and D. Pines. Phys. Rev. **92**, 609, (1953).
X. Ren, P. Rinke, C. Joas, and M. Scheffler. J. Mater. Sci., **47**, 7447, (2012).
- ⁶⁰ X. Ren, P. Rinke, C. Joas, and M. Scheffler. J. Mater. Sci., **47**, 7447, (2012).
- ⁶¹ A. V. Krukau, O. A. Vydrov, A. F. Izmaylov, and G. E. Scuseria, J. Chem. Phys. **125**, 224106 (2006).
- ⁶² P. E. Blöchl, C. F. J. Walther, and T. Pruschke, Phys. Rev. B **84**, 205101 (2011).
- ⁶³ M. Sotoudeh, S. Rajpurohit, P. E. Blöchl, D. Mierwald, J. Norpoth, V. Roddatis, S. Mildner, B. Kressdorf, B. Iffland, and C. Jooss, Phys. Rev. B **95**, 235150 (2017).
- ⁶⁴ A. Houari and F. Benissad, Adv. Theory Simul. **2**, 1900111 (2019).
- ⁶⁵ F. Benissad and A. Houari, Phys. Status Solidi B **258**, 2000241 (2020).
- ⁶⁶ M. Eckhoff, P. Blöchl, and J. Behler, Phys. Rev. B **101**, 205113 (2020).
- ⁶⁷ F. Allaoau, and A. Houari, *submitted to J. Phys: Cond. Matt* (2025).
- ⁶⁸ S. Rajpurohit, V. Vennelakanti, and H. J. Kulik, J. Phys. Chem. A **128**, 9082 (2024).
- ⁶⁹ V. L. Campo and M. Cococcioni, J. Phys. Condens. Matter **22**, 055602 (2010).
- ⁷⁰ V. I. Anisimov, J. Zaanen, and O. K. Andersen, Phys. Rev. B **44**, 943 (1991).
- ⁷¹ A. I. Liechtenstein, V. I. Anisimov, and J. Zaanen, Phys. Rev. B **52**, R5467 (1995).
- ⁷² S. Dudarev, G. Botton, S. Savrasov, C. Humphreys, and A. Sutton, Phys. Rev. B. **57**, 1505 (1998).
- ⁷³ I. Timrov, F. Aquilante, M. Cococcioni and N. Marzari Phys. Rev. X Energy **1**, 033003 (2022).
- ⁷⁴ O. Gunnarsson, O. Andersen, O. Jepsen, and J. Zaanen, Phys. Rev. B **39**, 1708 (1989).
- ⁷⁵ M. Hybertsen, M. Schlüter, and N. Christensen, Phys. Rev. B **39**, 9028 (1989).
- ⁷⁶ O. Gunnarsson, Phys. Rev. B **41**, 514 (1990).
- ⁷⁷ M. Springer and F. Aryasetiawan, Phys. Rev. B **57**, 4364 (1998).
- ⁷⁸ T. Kotani, J. Phys.: Condens. Matter **12**, 2413 (2000).
- ⁷⁹ F. Aryasetiawan, K. Karlsson, O. Jepsen, and U. Schönberger, Phys. Rev. B **74**, 125106 (2006).
- ⁸⁰ I. Timrov, N. Marzari, and M. Cococcioni, Phys. Rev. B **98**, 085127 (2018).
- ⁸¹ I. Timrov, N. Marzari, and M. Cococcioni, Phys. Rev. B **103**, 045141 (2021).
- ⁸² H. Kulik and N. Marzari, J. Chem. Phys. **129**, 134314 (2008).
- ⁸³ P. O. Löwdin, J. Chem. Phys. **18**, 365 (1950).
- ⁸⁴ Y. C. Wang, Z. H. Chen, and H. Jiang, J. Chem. Phys. **144**, 144106 (2016).
- ⁸⁵ J. Perdew, A. Ruzsinszky, G. Csonka, O. Vydrov, G. Scuseria, L. Constantin, X. Zhou, and K. Burke, Phys. Rev. Lett. **100**, 136406 (2008).
- ⁸⁶ V. I. Anisimov, I. V. Solovyev, M. A. Korotin, M. T. Czyżyk and G. A. Sawatzky, Phys. Rev. B **48**, 16929 (1993).
- ⁸⁷ M. T. Czyżyk and G. A. Sawatzky, Phys. Rev. B **49**, 14211 (1994).
- ⁸⁸ I. V. Solovyev, P. H. Dederichs, and V. I. Anisimov, Phys. Rev. B **50**, 16861 (1994).
- ⁸⁹ P. Giannozzi *et al.*, J. Phys.: Condens. Matter. **21**, 395502 (2009).
- ⁹⁰ P. Giannozzi *et al.*, J. Phys.: Condens. Matter **29**, 465901 (2017).
- ⁹¹ P. Giannozzi *et al.*, J. Chem. Phys. **152**, 154105 (2020).
- ⁹² P. E. Blöchl, Phys. Rev. B **50**, 17953 (1994).
- ⁹³ E. Kucukbenli, M. Monni, B. Adetunji, X. Ge, G. Ade-

- bayo, N. Marzari, S. de Gironcoli, and A. Dal Corso, arXiv:1404.3015 (2014).
- ⁹⁴ M. van Setten, M. Giantomassi, E. Bousquet, M. Verstraete, D. Hamann, X. Gonze, and G. M. Rignanese, *Comput. Phys. Commun.* **226**, 39 (2018).
- ⁹⁵ I. Timrov, N. Marzari, and M. Cococcioni, *Comput. Phys. Commun.* **279**, 108455 (2022).
- ⁹⁶ I. Mayer, *Int. J. Quant. Chem.* **90**, 63 (2002).
- ⁹⁷ H. J. Monkhorst and J. D. Pack, *Phys. Rev. B* **13**, 5188 (1976).
- ⁹⁸ N. Marzari, D. Vanderbilt, A. De Vita, and M. Payne, *Phys. Rev. Lett.* **82**, 3296 (1999).
- ⁹⁹ P. E. Blöchl, O. Jepsen, and O. K. Andersen, *Phys. Rev. B* **49**, 16223 (1994).
- ¹⁰⁰ <http://www.cppaw.org>
- ¹⁰¹ R. Car and M. Parrinello, *Phys. Rev. Lett.* **55**, 2471 (1985).
- ¹⁰² N. D. Mermin, *Phys. Rev.* **137**, A1441 (1965).
- ¹⁰³ F. Birch, *Phys. Rev.* **71**, 809 (1947).
- ¹⁰⁴ F. Tran, P. Blaha, K. Schwarz, and P. Novak, *Phys. Rev. B* **74**, 155108 (2006).
- ¹⁰⁵ P. Seth, P. Hansmann, A. van Roekeghem, L. Vaugier, and S. Biermann, *Phys. Rev. Lett.* **119**, 056401 (2017).
- ¹⁰⁶ S. Mandal, K. Haule, K. M. Rabe, and D. Vanderbilt *npj Computational Materials* **115** 11 (2019).
- ¹⁰⁷ H. M. Hong, Y. J. Kang, J. Kang, E. C. Lee, Y. H. Kim, and K. J. Chang, *Phys. Rev. B* **72**, 144408 (2005).